

Key Points:

- Guide field reduces energy conversion during magnetic reconnection
- An increase in background density and temperature leads to a decrease in energy conversion during magnetic reconnection
- Though guide field and background density and temperature affect energy conversion during magnetic reconnection, it still occurs mainly at reconnection front

Correspondence to:





S. Lu and Q. Lu,
lusan@ustc.edu.cn;
qmlu@ustc.edu.cn

Citation:

Shu, Y., Lu, S., Lu, Q., Wang, R., Zheng, J., & Ding, W. (2022). Effects of guide field and background density and temperature on energy conversion at magnetic reconnection front. *Journal of Geophysical Research: Space Physics*, 127, e2022JA030546. <https://doi.org/10.1029/2022JA030546>

Received 11 APR 2022
 Accepted 1 SEP 2022

Effects of Guide Field and Background Density and Temperature on Energy Conversion at Magnetic Reconnection Front

Yukang Shu¹ , San Lu^{2,3} , Quanming Lu^{2,3} , Rongsheng Wang^{2,3} , Jian Zheng¹ , and Weixing Ding¹

¹School of Nuclear Science and Technology, University of Science and Technology of China, Hefei, China, ²CAS Key Laboratory of Geospace Environment, School of Earth and Space Sciences, University of Science and Technology of China, Hefei, China, ³CAS Center for Excellence in Comparative Planetology, Hefei, China

Abstract Magnetic reconnection is a fundamental energy converting process changing the topology of the magnetic field in space. We investigate how the guide field and the background plasma density and temperature influence the energy converting process during magnetic reconnection using a two-dimensional particle-in-cell simulation code. It is shown that the guide field reduces both the reconnection rate and the energy conversion rate. Although the downstream Poynting flux from the reconnection site is enhanced during guide field magnetic reconnection, it does not participate in energy conversion as the inflow and outflow of Poynting flux from the left and right boundaries of the reconnection front cancel each other out. The major input of the Poynting flux participating in energy conversion comes from the upper and lower boundaries of the reconnection front. An electrostatic perturbing structure arises in cases with a strong guide field. Apart from the reconnection rate and the energy conversion rate, the energy outflow is altered by changing background plasma density and temperature. Our research shows that the energy input at a well-developed reconnection front in the case of the guide field does not come from the reconnection site, which implies the reconnection front can be an effective energy converter in the magnetosphere independent of the reconnection site once formed from the transient magnetic reconnection. These simulation results show that the guide field and background density and temperature quantitatively alter the energy conversion at the magnetic reconnection front, but the energy conversion pattern remains unchanged.

1. Introduction

As a fundamental energy converting process in space, magnetic reconnection is the key to understanding the coupling between the microscale kinetic process and the large-scale MHD process in the magnetosphere. When magnetic reconnection occurs, the magnetic field undergoes a topological change, and the free energy is released to plasmas (Birn & Priest, 2007; Yamada et al., 2010). Due to its ubiquitous presence, magnetic reconnection is often invoked as a promising source of explosive activities such as solar flares (Masuda et al., 1994), coronal mass ejection (Lin & Forbes, 2000), geomagnetic storms and substorms (Baker et al., 1996; Kepko et al., 2015). Furthermore, reconnection also plays a vital role in laboratory plasma facilities (Yamada et al., 1994).

Significant progress has been made in investigating the energy conversion at the reconnection site during magnetic reconnection. Birn and Hesse (2005) have shown that although magnetic reconnection is triggered in the diffusion region, which is merely several ion inertial lengths ($d_i \equiv c/\omega_{pi}$) wide, the energy conversion is not localized in the diffusion region. They also found that in contrast to the case in the classical resistive Sweet-Parker model, Joule and ohmic dissipation can be neglected in the overall energy transfer in the collisionless magnetic reconnection. The Poynting flux driven into the reconnection site from the inflow region is partially converted to the bulk kinetic flow and the enthalpy flux of plasmas; the rest part is diverted to the exhaust region, forming the pileup front. Satellite observations and numerical simulations have shown that outflow mainly consists of the Poynting flux and the enthalpy flux; the bulk kinetic flux commonly plays a minor role (Birn & Hesse, 2010; Eastwood et al., 2013). In addition, ion enthalpy flux is larger than the electron enthalpy flux in most cases, indicating that ions intend to gain more energy than electrons during the reconnection (Eastwood et al., 2013; Yamada et al., 2014, 2015; Zhong et al., 2019).

The energy converting process continues outside the diffusion region. The Poynting flux along with the plasma bulk flow (including bulk kinetic flux and enthalpy flux) forms reconnection fronts (also known as dipolarization fronts, characterized by an enhancement in B_z , and sometimes preceded by a small B_z dip) propagating downstream (Fu et al., 2013; Sitnov et al., 2009). Song et al. (2020) have examined the dynamics and energy balance of the reconnection front during formation. As another prominent energy converting region (Angelopoulos et al., 2013; Liu et al., 2014; Sitnov et al., 2018; Wang et al., 2020), the reconnection front constantly converts the magnetic energy to plasma energy (mainly enthalpy flux) through work by the electric field and the plasma pressure gradient force. Further simulation results and observation data indicate that intense energy converting process occurs at the front and may form the load ($\mathbf{J} \cdot \mathbf{E} > 0$) and generator ($\mathbf{J} \cdot \mathbf{E} < 0$) regions, which might be attributed to ballooning/interchange mode or lower hybrid drift instability (S. Y. Huang, Lu, et al., 2015; Khotyaintsev et al., 2017; Lapenta et al., 2014; Pritchett, 2015; Vapirev et al., 2013; Zhong et al., 2019).

Previous studies reported that energy conversion takes place both at the reconnection site and the reconnection front. Yi et al. (2019) found that the energy conversion rate (i.e., integration of $\mathbf{J} \cdot \mathbf{E}$ over the whole calculation region) does not peak simultaneously with the reconnection rate, and the integral work $\mathbf{J} \cdot \mathbf{E}$ at the reconnection front is much more efficient than at the reconnection site. Shu et al. (2021) also concluded that the reconnection rate cannot well reflect the energy converting process during the antiparallel reconnection, for the energy conversion mainly occurs at the reconnection front rather than the reconnection site. Besides, they found that the energy conversion at the well-developed reconnection front is unrelated to the reconnection site because the Poynting flux inflow mainly comes from the upper and lower direction of the front (through $\mathbf{E} \times \mathbf{B}$ drift) instead of straight from the reconnection site.

The guide field has been found to control the processes of magnetic reconnection, and the background density and temperature are also able to impact the reconnection process, but it is still unclear how they dictate the energy conversion, especially at the reconnection front. As a ubiquitous phenomenon in the magnetopause (Burch & Phan, 2016; Xu et al., 2020; Zhou et al., 2018), the magnetotail (Grigorenko et al., 2013; Nakamura et al., 2006; Zhou et al., 2019), and the magnetosheath (Zhong et al., 2022), the guide field reconnection is characterized by a reduced reconnection rate compared to the antiparallel reconnection (Ricci et al., 2004; Yi et al., 2019). Huba (2005) and Tharp et al. (2012) have given explanations for this reduction of the reconnection rate, reflecting the depressed energy conversion near the reconnection site. Formed near the reconnection site and driven by the magnetic tension force, the propagating reconnection front implies the connection between the reconnection site and the exhaust region. A thorough examination of the reduction in the energy conversion rate at the reconnection front is needed to illustrate the impact of the guide field on energy conversion during magnetic reconnection. Furthermore, the background density and temperature have also been found to modify the characteristics of magnetic reconnection (S. Lu, Angelopoulos, et al., 2019; S. Lu, Artemyev, et al., 2019; Wu & Shay, 2012; Wu et al., 2011).

To investigate how the guide field with varying intensities and the background plasma density and temperature influence the energy converting process during reconnection, we study the 2D PIC numerical simulations of both antiparallel reconnection with varying parameters of background density and temperature and component reconnection with different initial guide field values. Detailed analysis of energy budgets and comparison between different regimes are carried out.

The article is organized as follows. In Section 2, the numerical methods and the simulation setup are introduced, and results reflecting the effects of both guide field reconnection and background density and temperature are presented in Section 3. Discussion and conclusions will be given in Section 4.

2. Simulation Setup

A 2D explicit particle-in-cell (PIC) algorithm is applied in our research. The simulation is carried out in a box of $L_x \times L_z$, where $L_x = 204.8d_i$, $L_z = 25.6d_i$. The grid spacing is set to be $\Delta x = \Delta z = 0.05d_i$, and the time step is $\Delta t = 0.001\Omega_i^{-1}$. $\Omega_i = eB_0/m_i$ denotes the ion cyclotron frequency, where B_0 represents the asymptotic magnetic field. In our simulation, the mass ratio between ion and electron is set to be $m_i/m_e = 100$, and the speed of light is $c = 20V_A$, where $V_A = B_0/\sqrt{\mu_0 n_0 m_i}$ is the characteristic Alfvén velocity. We applied the periodic boundary conditions in the x -boundaries and perfect conductor boundary conditions in the z -boundaries.

Table 1
Parameters of Calculation Cases

| Case | B_{y0}/B_0 | n_b/n_0 | T_b/T_0 |
|------|--------------|-----------|-----------|
| A | 0 | 0.2 | 1 |
| B | 0.5 | 0.2 | 1 |
| C | 1 | 0.2 | 1 |
| D | 2 | 0.2 | 1 |
| E | 0 | 0.1 | 1 |
| F | 0 | 0.4 | 1 |
| G | 0 | 0.2 | 0.5 |
| H | 0 | 0.2 | 2.0 |

The initial configuration is a Harris current sheet equilibrium with a small perturbation to trigger the reconnection. The initial magnetic field is $\mathbf{B} = B_0 \tanh(z/\delta)\mathbf{e}_x + B_{y0}\mathbf{e}_y$, where B_{y0} is the uniform guide field, and $\delta = 0.5d_i$ is the half-width of the Harris current sheet. The plasma density is $n = n_0 \text{sech}^2(z/\delta) + n_b$, where n_0 is the peak n_b is the density of the background plasma. In our research, eight simulation cases with different parameters listed in Table 1 are performed to examine the influence of the guide field (Case A, B, C, D) and the background plasma density and temperature (Case A, E, F, G, H) on energy conversion.

3. Results

3.1. The Effects of Guide Field on Energy Conversion

The guide field shows a tendency of lowering the reconnection rate ($E_y/V_A B_0$ at the X-line) as it increases (solid lines in Figure 1), resulting in a lower growth rate of E_y at the reconnection front (dashed lines in Figure 1) (Q. Lu et al., 2013). The reduction of E_y at the reconnection front leads to the decrease of Poynting flux inflow from the z -direction ($E_y B_x/\mu_0$) and the local energy conversion $\mathbf{J}_y E_y$, finally depressing the total energy conversion during the reconnection (see the details in Figure 4).

To better quantify the energy conversion at specific regions during the guide field reconnection, we set three boxes (shown in Figure 2) circumventing the regions around the reconnection site (red), the reconnection front (blue), and the region ahead of the front (green), respectively. The box at the reconnection front enclosing the region where B_z is enhanced is of the same size as that at the reconnection site. When the reconnection front propagates downstream, both the boxes at the front and ahead of the front move along with it, while the box at the reconnection site is fixed. Figure 2 also depicts the distribution of energy conversion when the energy conversion rate (ECR, the integration of work $\mathbf{J} \cdot \mathbf{E}$ over the calculation domain) reaches maximum. It can be noticed that a perturbing structure ahead of the front arises and gets stronger when the guide field gets larger, which will be discussed later. From the integration of work over different regions shown in Figure 3, it can be concluded that energy conversion still dominantly takes place at the reconnection front (see blue lines in Figure 3) in the presence of the guide field. The integration of work at the reconnection site peaks earlier than at the reconnection front, while the energy conversion at the front can reach a higher value and lasts longer. Those results are consistent with the antiparallel reconnection. Nevertheless, as the guide field increases, energy conversion at the reconnection front descends. Meanwhile, the perturbation ahead of the front contributes negative work ($\mathbf{J} \cdot \mathbf{E} < 0$) on average in the later period of the guide field magnetic reconnection (see green lines in Figures 3b–3d).

Ions tend to gain less energy from the magnetic field under the influence of the guide field (see the details in Figure 4). The electron energy gain is also affected by the guide field, but the variation is less clear than ions. More specifically, the energy gain of electrons decreases as the guide field increases from 0 to B_0 (Figures 4a–4c), and then the energy gain becomes slightly higher as the guide field further increases to $2B_0$ (Figure 4d). The discrepancy between the two types of particles is more evident at the reconnection front where the ratio between $\mathbf{J}_i \cdot \mathbf{E}$ and $\mathbf{J}_e \cdot \mathbf{E}$ drops from five in the antiparallel case (Figures 4a) to 1.5 in the case of $B_{y0} = 2B_0$ (Figure 4d), indicating that the energy gain of ions is easier to be suppressed by the guide field.

The connection between electric field components and the energy conversion can be described using these two equations:

$$\frac{\partial}{\partial t} \frac{B_x^2 + B_z^2}{2\mu_0} + \frac{1}{\mu_0} \left[\frac{\partial(E_y B_z)}{\partial x} - \frac{\partial(E_y B_x)}{\partial z} \right] = -J_y E_y \quad (1)$$

$$\frac{\partial}{\partial t} \frac{B_y^2}{2\mu_0} + \frac{1}{\mu_0} \left[\frac{\partial(E_x B_y)}{\partial z} - \frac{\partial(E_z B_y)}{\partial x} \right] = -J_x E_x - J_z E_z \quad (2)$$

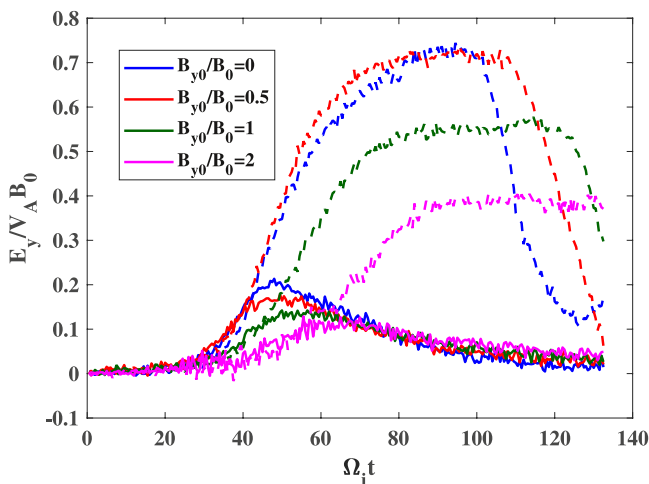


Figure 1. Evolution of E_y over time near the reconnection site (solid lines) and at the reconnection front (dashed lines) in cases with different initial guide fields.

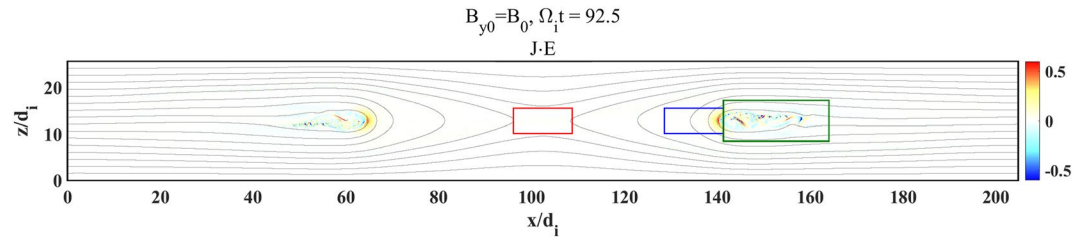


Figure 2. Profile of work $\mathbf{J} \cdot \mathbf{E}$ at $\Omega_1 t = 92.5$ (when the energy conversion rate reaches a maximum) with guide field $B_{y0} = B_0$, gray lines represent the magnetic field lines. Two boxes of the same size are set at the reconnection site (red) and the reconnection front (blue) for better quantification. Another green box marks the area ahead of the front enclosing the perturbing structure. Notice that the blue box and the green box move along with the reconnection front as it propagates downward.

As shown in Equation 1, the out-of-plane component of the electric field E_y is connected to the in-plane components of the magnetic field. Correspondingly, the guide field B_y is related to the alteration of in-plane components of the electric field (Equation 2). Those equations can be derived from Maxwell's equations (shown in Appendix A), considering that $\partial/\partial y$ is reduced to zero in the two-dimensional configuration, and the energy density of the electric field is negligible. One may find that by combining Equations 1 and 2, we can obtain Poynting's theorem:

$$\frac{1}{2\mu_0} \frac{\partial B^2}{\partial t} + \nabla \cdot \mathbf{S} = -\mathbf{J} \cdot \mathbf{E} \quad (3)$$

In the antiparallel case, the energy conversion is dominated by $J_y E_y$ constricted at the reconnection front (see the first row in Table 3); the energy input at the reconnection front mainly comes from the z -direction (see the first row in Table 2), and terms in Equation 2 are almost zero (see the first row in Table 4). In the guide field case, $J_y E_y$ still concentrates at the reconnection front (Figure 5b) but is depressed. As the guide field gets larger, the terms related to B_y in Equation 2 begin to grow (e.g., $E_z B_y / \mu_0$ as a part of S_x shown in Figure 5a and in-plane energy conversion $J_x E_x + J_z E_z$ ahead of the front in Figure 5c). As shown in Table 2, even though S_x is enhanced during the guide field reconnection, the inflow S_x from the left boundary (x_1) is nearly canceled by the outflow from the right boundary (x_2). Thus, the overall energy input at the front still comes from S_z in the z -direction (F_{z1} and F_{z2} in Table 2), which shows slight asymmetry at the upper and lower boundaries in the presence of the guide field.

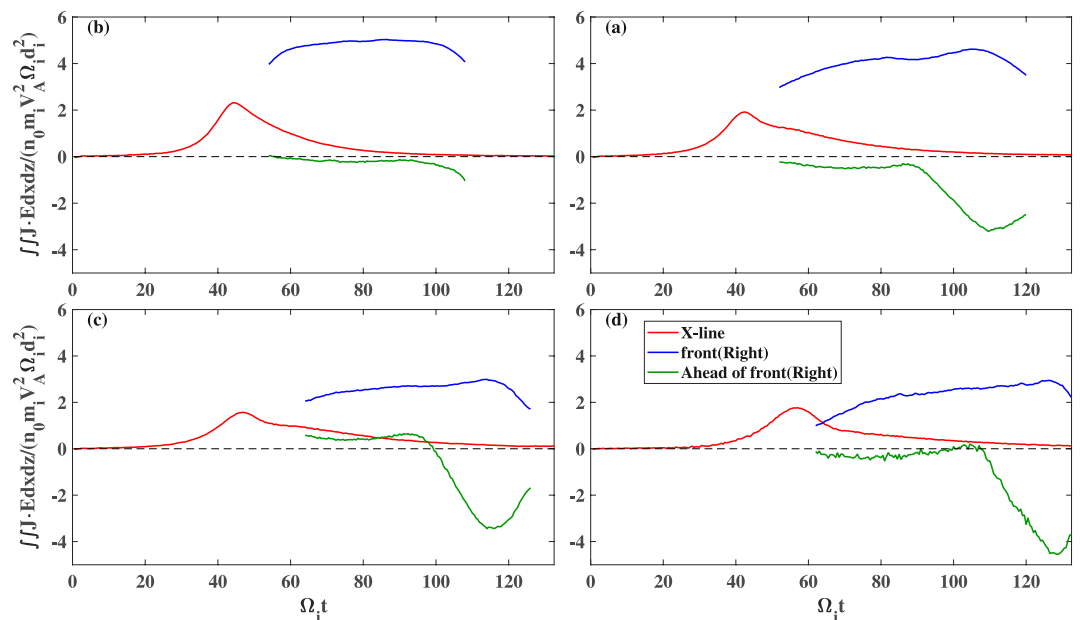


Figure 3. Integration of work $\mathbf{J} \cdot \mathbf{E}$ over regions of the reconnection site, the reconnection front and regions ahead of the front (boxes in Figure 2) when (a) $B_{y0} = 0$, (b) $B_{y0} = 0.5B_0$, (c) $B_{y0} = B_0$, (d) $B_{y0} = 2B_0$.

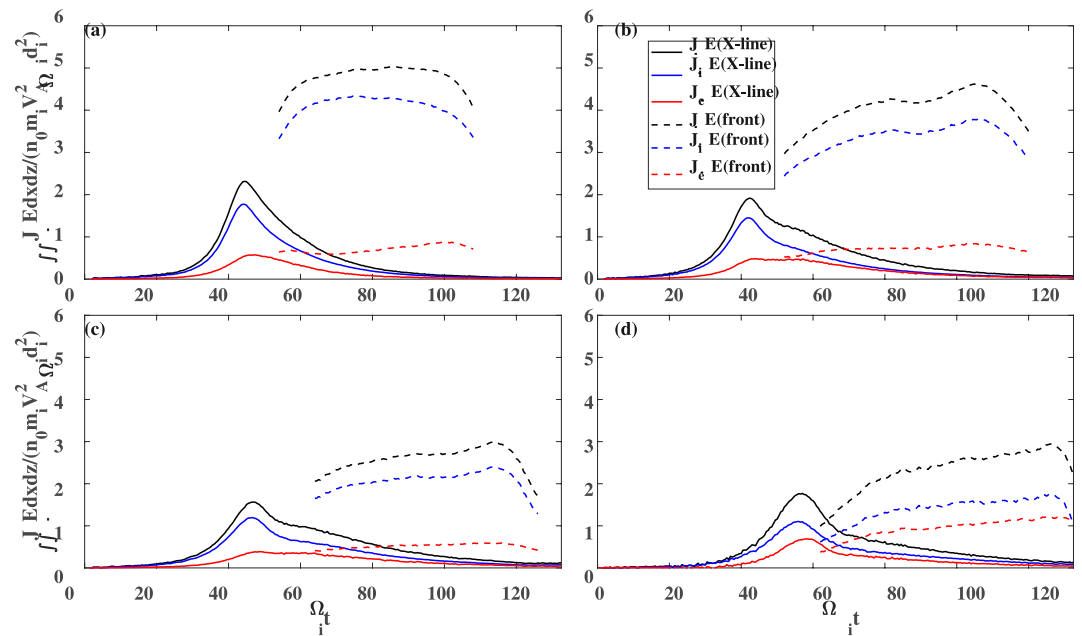


Figure 4. Integration of work by the electric field on electrons ($\mathbf{J}_e \cdot \mathbf{E}$), ions ($\mathbf{J}_i \cdot \mathbf{E}$), and plasmas ($\mathbf{J} \cdot \mathbf{E}$) at the reconnection site and the front over boxes at both places, respectively (see Figure 2) under different guide fields. Solid lines represent the work at the reconnection site and dashed lines for the front. (a) $B_{y0} = 0$, (b) $B_{y0} = 0.5 B_0$, (c) $B_{y0} = B_0$, (d) $B_{y0} = 2 B_0$.

As the guide field gets stronger, S_z (more specifically, the $E_y B_x / \mu_0$ component of S_z) also decreases as well as the out-of-plane component of work $J_y E_y$ (Table 3).

It can be noticed in Table 4 that components of Poynting flux related to B_y arise with the guide field, especially when the guide field is large ($B_{y0} = 2 B_0$). At the same time, the in-plane perturbation $J_x E_x + J_z E_z$ ahead of the front begins to influence the energy conversion at the reconnection front.

The components of work plotted along the neutral line (marked as the red dashed line in Figure 5c) with different guide fields verify this tendency. The perturbation emerges ahead of the front with the guide field and reaches the same level with the $J_y E_y$ component when $B_{y0} = 2 B_0$ (Figure 6d). The in-plane electric field components are decomposed into the electrostatic part $-\nabla\phi$ and the electromagnetic part $-\partial\mathbf{A}/\partial t$ under the Coulomb gauge via solving Poisson's equation (S. Lu et al., 2021). It can be seen that the electrostatic part of the electric field (Figures 7b and 7e) is much larger than the electromagnetic part (Figures 7c and 7f), which proves that the perturbation is electrostatic.

Apart from decreasing the energy conversion, the guide field also diverts the flow direction and changes the distribution of the energy flux. At the exhaust region near the reconnection site, the outflow of the plasma kinetic energy flux (Figures 8b and 8e) and the enthalpy flux (Figures 8c and 8f) display an antisymmetric structure. It is worth noting that the electron kinetic energy flux is distributed at the separatrices (Figure 8e), along with a stream of perturbing Poynting flux (Figures 8a and 8d), which is likely to be related to electron holes (Chang et al., 2021; C. Huang et al., 2014; Hutchinson, 2017; Lapenta et al., 2010; Q. M. Lu et al., 2008). At the reconnection front, the asymmetry still holds in the kinetic energy flux and the enthalpy flux (Figures 9c–9f). Those energy fluxes tend to flow in the upper right direction at the right side of the X-line owing to the Lorentz force $J_{ix} B_y$ on ions provided by the guide field. The electron outflow at the exhaust region accompanies the ion flow due to the quasi-neutral condition.

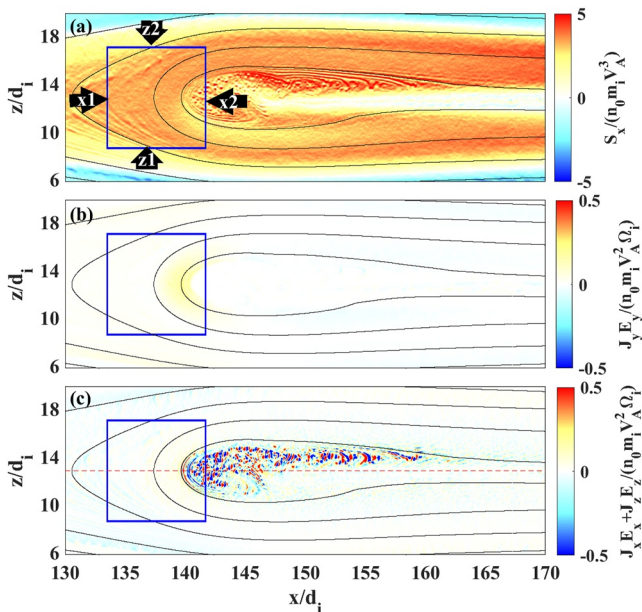


Figure 5. (a) x -component of Poynting flux, (b) out-of-plane component, and (c) in-plane component of work by the electric field around the reconnection front region at $\Omega_i t = 104.5$ with $B_{y0} = 2 B_0$. The black lines represent the magnetic field lines. The blue box includes the reconnection front where B_z reaches maximum.

Table 2

The Inflow of Poynting Flux From Four Boundaries of the Box (Figure 5a) Enclosing the Reconnection Front, Measured When the ECR Reaches Its Peak With Different Initial Guide Fields

| B_{y0} | F_{x1} | F_{x2} | F_{z1} | F_{z2} | Total |
|----------|----------|----------|----------|----------|-------|
| 0 | -0.018 | 1.309 | 1.894 | 1.898 | 5.083 |
| 0.5 | 1.364 | -0.699 | 1.846 | 1.810 | 4.321 |
| 1.0 | 2.346 | -2.626 | 1.618 | 1.260 | 2.598 |
| 2.0 | 11.340 | -12.202 | 1.855 | 1.378 | 2.371 |

Note. The results are averaged over $\pm 5\Omega_i^{-1}$. The moving velocity of the box has been considered. $F_{x1} = \int S_x dz / (n_0 m_i V_A^3 d_i)$, $F_{x2} = \int -S_x dz / (n_0 m_i V_A^3 d_i)$, $F_{z1} = \int S_z dx / (n_0 m_i V_A^3 d_i)$, $F_{z2} = \int -S_z dx / (n_0 m_i V_A^3 d_i)$, where x_1 , x_2 , z_1 , and z_2 are different boundaries marked in Figure 5a, respectively.

3.2. The Effects of the Background Plasma Density and Temperature on Energy Conversion

The maximum reconnection rate can be altered by the background plasma density and temperature. Through several examples, we show that both background density and background temperature have a negative correlation with the maximum reconnection rate (Figure 10a) and the energy conversion rate (Figure 10b). For the same background temperature, higher background density will lead to lower maximum reconnection rate and ECR (see the blue, black, and red lines in Figures 10a and 10b). When fixing the background density, the increment of the background temperature can also lead to lower maximum reconnection rate and ECR (the green, black, and magenta lines in Figures 10a and 10b). As for the same plasma β , the impact of the background density on energy conversion is larger than the background temperature, for example, the maximum reconnection rate and ECR of Case E (the blue lines in Figures 10a and 10b, the background density is reduced by half compared with Case A) are higher than Case G (the green lines in Figures 10a and 10b, the background temperature is reduced by half), even though the plasma β is same for both cases. Likewise for Case F (the red lines in Figure 10) and Case H (the magenta lines in Figure 10).

The outflow energy flux at the reconnection front is also influenced by the background plasma. As shown in Figure 11, the Poynting flux (see the blue lines in Figures 11a–11c) and the ion kinetic energy flux (see the red lines in Figures 11a–11c) are inversely correlated with the background density. Likewise, those energy fluxes are also influenced by the background temperature (Figures 11d–11f). Besides, the ion enthalpy flux outflow is slightly weakened as the background temperature rises (see the green lines in Figures 11d–11f).

4. Conclusions and Discussion

In this study, we investigated the influence of the guide field and the background density and temperature on the energy conversion of magnetic reconnection via 2D PIC simulation. Our major findings are listed as follows:

1. A large initial guide field ($B_g \geq B_0$) can decrease the growth rate of the reconnection rate, thus reducing the out-of-plane component of the electric field at the pileup region, which forms the reconnection front. As a result, the components of Poynting fluxes and energy conversion essentially participating in the energy conversion decrease, as they are closely related to the out-of-plane electric field component. The downstream Poynting flux straight from the reconnection site has a small impact on the overall energy conversion, even though it grows larger as the initial guide field increases.
2. When the guide field increases, ions gain less energy from the electromagnetic field. The electron energy gain decreases as the guide field increases from 0 to B_0 but then increases slightly as the guide field increases to $2B_0$. The variation of the electron energy gain is weaker than ions.
3. Energy conversion occurs primarily at the reconnection front. However, as the guide field increases, an electrostatic perturbation with localized loads ($\mathbf{J} \cdot \mathbf{E} > 0$) and generators ($\mathbf{J} \cdot \mathbf{E} < 0$) occurs in the region ahead of the front, whose integral contribution to the energy conversion is negative.
4. The energy fluxes (Poynting flux, electron/ion kinetic energy flux, and enthalpy flux) in the exhaust region are diverted by the guide field, which show an asymmetric structure.
5. The increase in the background density and temperature reduces the reconnection rate, the energy conversion rate, and the outflow of the energy fluxes (especially the Poynting flux and the ion kinetic energy flux). Furthermore, the impact of background density on energy conversion is stronger than the background temperature for the same plasma β .

Note that E_y at the reconnection front in Figure 1 does not decrease significantly when the guide field B_{y0} increases from 0 to $0.5B_0$, but when the guide field further increases to $B_{y0} \geq B_0$, the energy conversion differs from those with lower guide fields. This is consistent with previous simulation results by Pucci et al. (2018), which showed that the energy transfer in magnetic

Table 3

Integration of Terms in Equation 1 Over the Box in Figure 5 at the Peak of ECR

| B_{y0}/B_0 | $\frac{\partial(B_x^2+B_z^2)}{\partial t} / 2\mu_0$ | $\frac{\partial(E_y B_z)}{\mu_0 \partial x}$ | $-\frac{\partial(E_y B_x)}{\mu_0 \partial z}$ | $J_y E_y$ |
|--------------|---|--|---|-----------|
| 0 | -0.7571 | -0.0929 | -3.7960 | 5.0073 |
| 0.5 | 0.4265 | -0.1795 | -3.7232 | 4.0881 |
| 1.0 | -0.1190 | 0.1260 | -2.5979 | 2.9003 |
| 2.0 | -0.0702 | 0.0110 | -1.5118 | 2.1640 |

Note. Those integrated terms are normalized by $(n_0 m_i V_A^2 \Omega_i d_i^2)$. The results are averaged over $\pm 5\Omega_i^{-1}$. The moving velocity of the box has been considered.

Table 4
Integration of Terms in Equation 2 Over the Box in Figure 5 at the Peak of ECR

| B_{y0}/B_0 | $\frac{\partial B_y^2}{\partial t} \frac{1}{2\mu_0}$ | $\frac{\partial(E_x B_y)}{\mu_0 \partial z}$ | $-\frac{\partial(E_z B_y)}{\mu_0 \partial x}$ | $J_z E_z + J_x E_x$ |
|--------------|--|--|---|---------------------|
| 0 | 0.0003 | 0.0114 | 0.0102 | -0.0228 |
| 0.5 | 0.0230 | 0.0832 | -0.2896 | 0.1189 |
| 1.0 | -0.0786 | -0.3646 | 0.7916 | -0.2122 |
| 2.0 | 0.3033 | -1.9132 | 1.0641 | 0.4301 |

Note. Those integrated terms are normalized by $(n_0 m_i V_A^2 \Omega_i d_i^2)$. The results are averaged over $\pm 5\Omega_i^{-1}$. The moving velocity of the box has been considered.

reconnection can be separated into two regimes by a threshold guide field ($B_{y0,th} \sim 0.6B_0$).

Our simulations show that when the guide field is large, a perturbation structure is formed ahead of the reconnection front with loads and generators in energy conversion $\mathbf{J} \cdot \mathbf{E}$, and we show that this structure is purely electrostatic (see Figure 7). This structure may be generated by the electron Kelvin-Helmholtz instability because of the electron velocity shear (Che & Zank, 2020; Fermo et al., 2012; C. Huang, Lu, et al., 2015) or the lower hybrid drift instability (Divin et al., 2015; Khotyaintsev et al., 2017; Yoon & Lui, 2008), which is worthy of further investigations.

Our results on the effects of background density and temperature are consistent with conclusions by Lu et al. (2019a). They also proposed that the outflow velocity decreases as the background density or temperature ascends, which

is also found in our simulation results that the propagation velocity of the reconnection front drops as the background plasma density or temperature increases. For the guide field cases, the variation of the front moving speed does not exceed 10%.

Our calculations at the reconnection front are based on the approximation that the front moves downstream with a constant velocity, which has been already verified for the antiparallel case. The approximation still holds in the existence of a guide field. The mass ratio in our simulation is set to be 100. Variation of the mass ratio might change the ratio between the ion and electron energy gain. In other particle-in-cell simulations, it is found that the guide field might raise the electron energy gain although the total energy conversion still drops (Pucci et al., 2018; Yi et al., 2020). We set a small initial perturbation in the middle of the calculation domain to ensure the single X-line configuration. During the calculation time, the reconnection front does not reach the boundaries in the x -direction, eliminating the effects of the magnetic island from the periodic boundary.

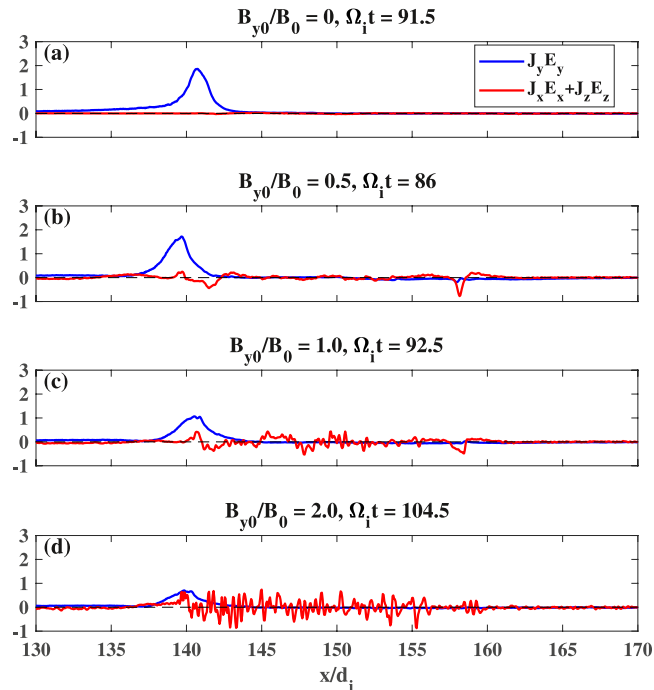


Figure 6. Integration of the out-of-plane component $J_y E_y$ (blue) and in-plane components $J_x E_x + J_z E_z$ (red) of work from $z = 10.1d_i$ to $z = 15.5d_i$ at the neutral line (the red dashed line in Figure 5c) with different guide fields at the time when the ECR reaches its peak. The integrated terms are normalized by $(n_0 m_i V_A^2 \Omega_i d_i)$.

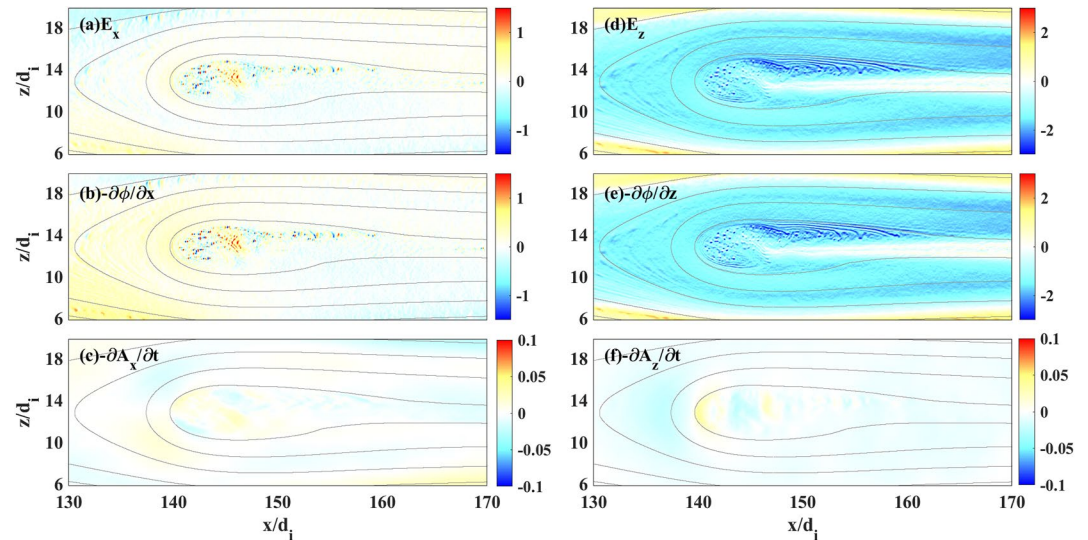


Figure 7. The decomposition of the electric field components (a) E_x and (d) E_z via solving Poisson's equation. (b) and (e) the electrostatic part. (c) and (f) the electromagnetic part. $\Omega_i t = 104.5$, $B_{y0} = 2B_0$.

Our 2D simulation has its limitations that energy transferring modes are constricted in the xz -plane. The magnetic reconnection, especially with a guide field is naturally a 3D configuration. Some instabilities or wave modes such as the fluctuating structure by the ballooning mode mentioned above can only be observed in the 3D results. It is also intriguing whether the perturbation ahead of the front in our results has a connection with those 3D turbulent modes in 3D configuration, which drives our future research on energy conversion into the 3D regime.

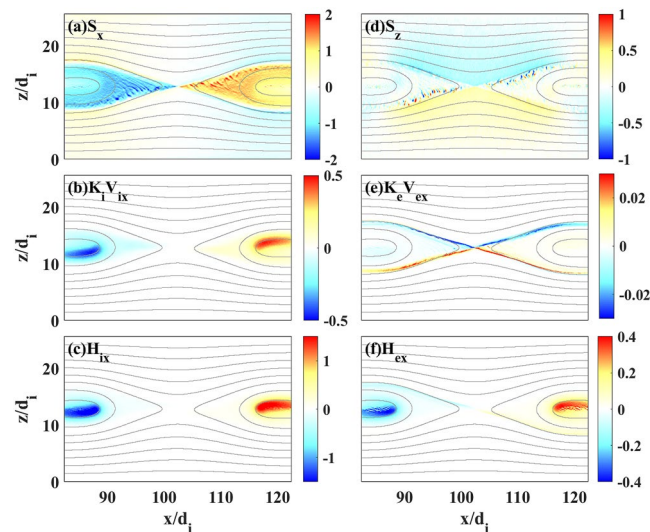


Figure 8. Energy flux outflow near the reconnection site: components of the Poynting flux (a) S_x and (d) S_z , (b) the ion kinetic energy flux $K_i V_{ix}$, (e) the electron kinetic energy flux $K_e V_{ex}$, (c) the ion enthalpy flux H_{ix} , and (f) the electron enthalpy flux H_{ex} . $B_{y0} = B_0$, $\Omega_i t = 60$.

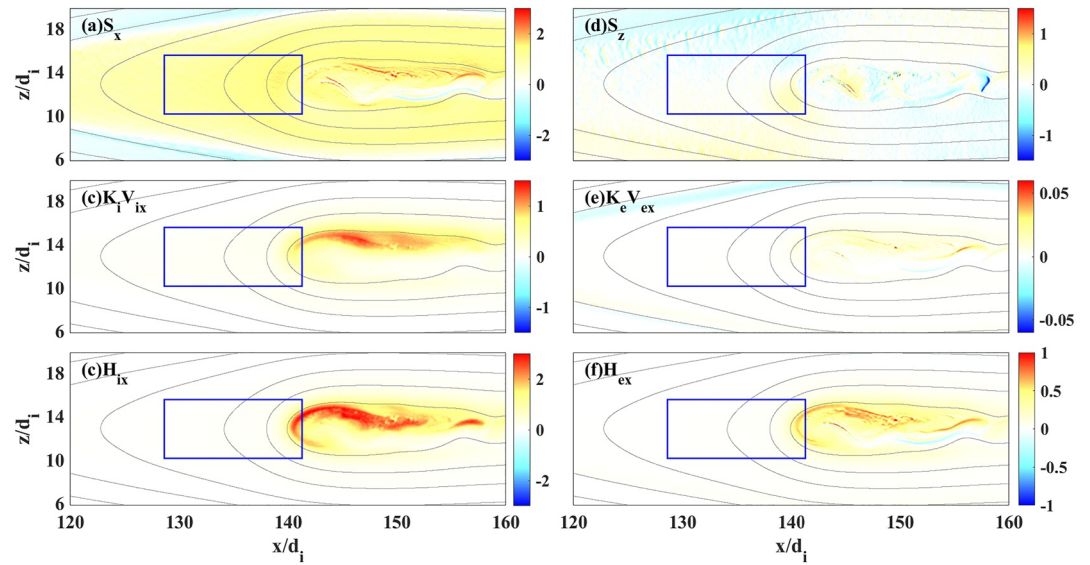


Figure 9. Energy flux outflow around the reconnection front: components of the Poynting flux (a) S_x and (d) S_z , (b) the ion kinetic energy flux $K_i V_{ix}$, (e) the electron kinetic energy flux $K_e V_{ex}$, (c) the ion enthalpy flux H_{ix} , and (f) the electron enthalpy flux H_{ex} . $B_{y0} = B_0$, $\Omega_i t = 92.5$. The blue box marks the area of the reconnection front where the B_z component reaches maximum.

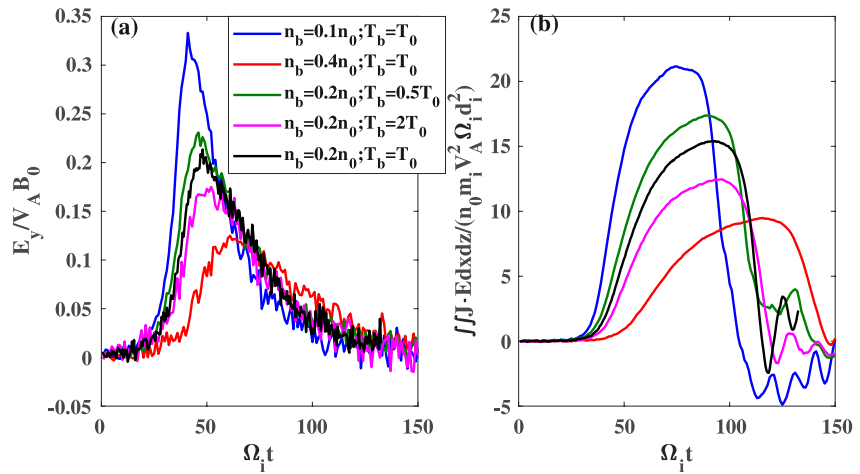


Figure 10. The evolution of (a) the reconnection rate $E_y/V_A B_0$ and (b) the energy conversion rate with different background plasma densities and temperatures.

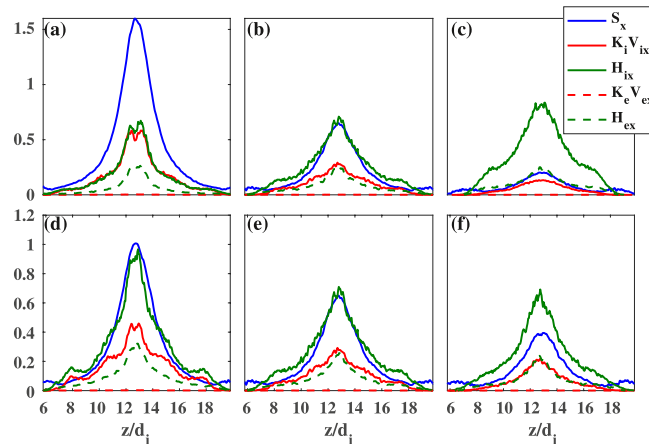


Figure 11. Plots of the energy outflow at the reconnection front with different background plasma parameters at the time when the ECR reaches maximum. (a) $n_b = 0.1n_0$, $T_b = T_0$; (b) $n_b = 0.2n_0$, $T_b = T_0$; (c) $n_b = 0.4n_0$, $T_b = T_0$; (d) $n_b = 0.2n_0$, $T_b = 0.5T_0$; (e) $n_b = 0.2n_0$, $T_b = T_0$; (f) $n_b = 0.2n_0$, $T_b = 2T_0$.

Appendix A: Derivation of Equations 1 and 2

We write the component equations of two of Maxwell's equations below, considering that the derivative $\partial/\partial y = 0$ in the xz -plane.

$$\frac{\partial \mathbf{B}}{\partial t} = -\nabla \times \mathbf{E}$$

$$\frac{1}{c^2} \frac{\partial \mathbf{E}}{\partial t} = \nabla \times \mathbf{B} - \mu_0 \mathbf{J}$$

We have

$$\frac{\partial B_y}{\partial t} = \frac{\partial E_z}{\partial x} - \frac{\partial E_x}{\partial z} \quad (\text{A1})$$

$$\frac{\partial B_x}{\partial t} = \frac{\partial E_y}{\partial z} \quad (\text{A2})$$

$$\frac{\partial B_z}{\partial t} = -\frac{\partial E_y}{\partial x} \quad (\text{A3})$$

$$\frac{1}{c^2} \frac{\partial E_y}{\partial t} = \frac{\partial B_x}{\partial z} - \frac{\partial B_z}{\partial x} - \mu_0 J_y \quad (\text{A4})$$

$$\frac{1}{c^2} \frac{\partial E_x}{\partial t} = -\frac{\partial B_y}{\partial z} - \mu_0 J_x \quad (\text{A5})$$

$$\frac{1}{c^2} \frac{\partial E_z}{\partial t} = \frac{\partial B_y}{\partial x} - \mu_0 J_z \quad (\text{A6})$$

Combining those equations through $B_y \cdot (\text{A1}) + E_x \cdot (\text{A5}) + E_z \cdot (\text{A6})$, we can get

$$\frac{\partial}{\partial t} \left(\frac{B_y^2}{2\mu_0} + \epsilon_0 \frac{E_x^2 + E_z^2}{2} \right) + \frac{1}{\mu_0} \left[\frac{\partial (E_x B_y)}{\partial z} - \frac{\partial (E_z B_y)}{\partial x} \right] = -J_x E_x - J_z E_z \quad (\text{A7})$$

And by $B_x \cdot (\text{A2}) + B_z \cdot (\text{A3}) + E_y \cdot (\text{A4})$, we get

$$\frac{\partial}{\partial t} \left(\frac{B_x^2 + B_z^2}{2\mu_0} + \epsilon_0 \frac{E_y^2}{2} \right) + \frac{1}{\mu_0} \left[\frac{\partial (E_y B_z)}{\partial x} - \frac{\partial (E_y B_x)}{\partial z} \right] = -J_y E_y \quad (\text{A8})$$

The electric energy density $\epsilon_0 E^2/2$ is negligible compared to magnetic energy density. Thus, we omit the terms of electric energy density and get Equations 1 and 2 in the main text. Combining Equations A7 and A8, we can get the Poynting equation

$$\frac{\partial}{\partial t} \left(\frac{1}{2\mu_0} B^2 + \frac{\epsilon_0}{2} E^2 \right) + \nabla \cdot \mathbf{S} = \mathbf{J} \cdot \mathbf{E}$$

It should be noticed that only under the condition of two-dimensional configuration ($\partial/\partial y$ is reduced to zero), the Poynting equation can be divided into decoupled “component forms” as Equations A7 and A8. Equation A7 shows that the out-of-plane magnetic field component (namely, the guide field) is connected with the in-plane electric field components. Correspondingly, the in-plane magnetic field components are related to the out-of-plane electric field, as in Equation A8.

Data Availability Statement

The simulation data for the figures and tables in the paper can be downloaded from <https://dx.doi.org/10.12176/01.99.02651>.

Acknowledgments

This work was supported by the Strategic Priority Research Program of Chinese Academy of Sciences, Grant No. XDB 41000000, the NSFC Grant 42174181. Grateful acknowledgment is made to the data resources from “National Space Science Data Center, National Science and Technology Infrastructure of China (<http://www.nssdc.ac.cn>).” The simulation results described in Section 3 are generated from our computer simulation model. Moreover, the simulation model is described in Section 2.

References

- Angelopoulos, V., Runov, A., Zhou, X. Z., Turner, D. L., Kiehas, S. A., Li, S. S., & Shinohara, I. (2013). Electromagnetic energy conversion at reconnection fronts. *Science*, *341*(6153), 1478–1482. <https://doi.org/10.1126/science.1236992>
- Baker, D. N., Pulkkinen, T. I., Angelopoulos, V., Baumjohann, W., & McPherron, R. L. (1996). Neutral line model of substorms: Past results and present view. *Journal of Geophysical Research*, *101*(A6), 12975–13010. <https://doi.org/10.1029/95JA03753>
- Birn, J., & Hesse, M. (2005). Energy release and conversion by reconnection in the magnetotail. *Annales Geophysicae*, *23*(10), 3365–3373. <https://doi.org/10.5194/angeo-23-3365-2005>
- Birn, J., & Hesse, M. (2010). Energy release and transfer in guide field reconnection. *Physics of Plasmas*, *17*(1), 1–11. <https://doi.org/10.1063/1.3299388>
- Birn, J., & Priest, E. R. (2007). *Reconnection of magnetic fields*. Cambridge University Press. <https://doi.org/10.1086/171911>
- Burch, J. L., & Phan, T. D. (2016). Magnetic reconnection at the dayside magnetopause: Advances with MMS. *Geophysical Research Letters*, *43*(16), 8327–8338. <https://doi.org/10.1002/2016GL069787>
- Chang, C., Huang, K., Lu, Q., Sang, L., Lu, S., Wang, R., et al. (2021). Particle-in-cell simulations of electrostatic solitary waves in asymmetric magnetic reconnection. *Journal of Geophysical Research: Space Physics*, *126*(7), 1–11. <https://doi.org/10.1029/2021JA029290>
- Che, H., & Zank, G. P. (2020). Electron acceleration from expanding magnetic vortices during reconnection with a guide field. *The Astrophysical Journal*, *889*(1), 11. <https://doi.org/10.3847/1538-4357/ab5d3b>
- Divin, A., Khotyaintsev, Y. V., Vaivads, A., André, M., Markidis, S., & Lapenta, G. (2015). Evolution of the lower hybrid drift instability at reconnection jet front. *Journal of Geophysical Research - A: Space Physics*, *120*(4), 2675–2690. <https://doi.org/10.1002/2014JA020503>
- Eastwood, J. P., Phan, T. D., Drake, J. F., Shay, M. A., Borg, A. L., Lavraud, B., & Taylor, M. G. G. T. (2013). Energy partition in magnetic reconnection in earth’s magnetotail. *Physical Review Letters*, *110*(22), 1–5. <https://doi.org/10.1103/PhysRevLett.110.225001>
- Fermo, R. L., Drake, J. F., & Swisdak, M. (2012). Secondary magnetic islands generated by the Kelvin-Helmholtz instability in a reconnecting current sheet. *Physical Review Letters*, *108*(25), 1–5. <https://doi.org/10.1103/PhysRevLett.108.255005>
- Fu, H. S., Cao, J. B., Khotyaintsev, Y. V., Sitnov, M. I., Runov, A., Fu, S. Y., et al. (2013). Dipolarization fronts as a consequence of transient reconnection: In situ evidence. *Geophysical Research Letters*, *40*(23), 6023–6027. <https://doi.org/10.1002/2013GL058620>
- Grigorenko, E. E., Malova, H. V., Artemyev, A. V., Mingalev, O. V., Kronberg, E. A., Koleva, R., et al. (2013). Current sheet structure and kinetic properties of plasma flows during a near-Earth magnetic reconnection under the presence of a guide field. *Journal of Geophysical Research: Space Physics*, *118*(6), 3265–3287. <https://doi.org/10.1002/jgra.50310>
- Huang, C., Lu, Q., Guo, F., Wu, M., Du, A., & Wang, S. (2015). Magnetic islands formed due to the Kelvin-Helmholtz instability in the outflow region of collisionless magnetic reconnection. *Geophysical Research Letters*, *42*(18), 7282–7286. <https://doi.org/10.1002/2015GL065690>
- Huang, C., Lu, Q., Wang, P., Wu, M., & Wang, S. (2014). Characteristics of electron holes generated in the separatrix region during antiparallel magnetic reconnection. *Journal of Geophysical Research: Space Physics*, *119*(8), 6445–6454. <https://doi.org/10.1002/2014JA019991>
- Huang, S. Y., Fu, H. S., Yuan, Z. G., Zhou, M., Fu, S., Deng, X. H., et al. (2015). Electromagnetic energy conversion at dipolarization fronts: Multispacecraft results. *Journal of Geophysical Research: Space Physics*, *120*(6), 1–24. <https://doi.org/10.1002/2015JA021094>. Received
- Huba, J. D. (2005). Hall magnetic reconnection: Guide field dependence. *Physics of Plasmas*, *12*(1), 1–6. <https://doi.org/10.1063/1.1834592>
- Hutchinson, I. H. (2017). Electron holes in phase space: What they are and why they matter. *Physics of Plasmas*, *24*(5), 055601. <https://doi.org/10.1063/1.4976854>
- Kepko, L., McPherron, R. L., Amm, O., Apatenkov, S., Baumjohann, W., Birn, J., et al. (2015). Substorm current wedge revisited. *Space Science Reviews*, *190*(1–4), 1–46. <https://doi.org/10.1007/s11214-014-0124-9>
- Khotyaintsev, Y. V., Divin, A., Vaivads, A., André, M., & Markidis, S. (2017). Energy conversion at dipolarization fronts. *Geophysical Research Letters*, *44*(3), 1234–1242. <https://doi.org/10.1002/2016GL071909>
- Lapenta, G., Goldman, M. V., Newman, D. L., Markidis, S., & Divin, A. (2014). Electromagnetic energy conversion in downstream fronts from three dimensional kinetic reconnection. *Physics of Plasmas*, *21*(5), 055702. <https://doi.org/10.1063/1.4872028>
- Lapenta, G., Markidis, S., Divin, A., Goldman, M. V., & Newman, D. L. (2010). Scales of guide field reconnection at the hydrogen mass ratio. *Physics of Plasmas*, *17*(8), 082106. <https://doi.org/10.1063/1.3467503>
- Lin, J., & Forbes, T. G. (2000). Effects of reconnection on the coronal mass ejection process. *Journal of Geophysical Research*, *105*(A2), 2375–2392. <https://doi.org/10.1029/1999ja900477>

- Liu, J., Angelopoulos, V., Zhou, X.-Z., & Runov, A. (2014). Magnetic flux transport by dipolarizing flux bundles. *Journal of Geophysical Research: Space Physics*, *119*(2), 909–926. <https://doi.org/10.1002/2013JA019395>
- Lu, Q., Lu, S., Huang, C., Wu, M., & Wang, S. (2013). Self-reinforcing process of the reconnection electric field in the electron diffusion region and onset of collisionless magnetic reconnection. *Plasma Physics and Controlled Fusion*, *55*(8), 085019. <https://doi.org/10.1088/0741-3335/55/8/085019>
- Lu, Q. M., Lembege, B., Tao, J. B., & Wang, S. (2008). Perpendicular electric field in two-dimensional electron phase-holes: A parameter study. *Journal of Geophysical Research*, *113*(11), 1–17. <https://doi.org/10.1029/2008JA013693>
- Lu, S., Angelopoulos, V., Artemyev, A. V., Pritchett, P. L., Liu, J., Runov, A., et al. (2019). Turbulence and particle acceleration in collisionless magnetic reconnection: Effects of temperature inhomogeneity across pre-reconnection current sheet. *The Astrophysical Journal*, *878*(2), 109. <https://doi.org/10.3847/1538-4357/ab1f6b>
- Lu, S., Angelopoulos, V., Pritchett, P. L., Nan, J., Huang, K., Tao, X., et al. (2021). Electrodynamic contributions to the Hall- and parallel electric fields in collisionless magnetic reconnection. *Journal of Geophysical Research: Space Physics*, *126*(11), 1–10. <https://doi.org/10.1029/2021JA029550>
- Lu, S., Artemyev, A. V., Angelopoulos, V., Pritchett, P. L., & Runov, A. (2019). Effects of cross-sheet density and temperature inhomogeneities on magnetotail reconnection. *Geophysical Research Letters*, *46*(1), 28–36. <https://doi.org/10.1029/2018GL081420>
- Masuda, S., Kosugi, T., Hara, H., Tsuneta, S., & Ogawara, Y. (1994). A loop-top hard X-ray source in a compact solar flare as evidence for magnetic reconnection. *Nature*, *371*(6497), 495–497. <https://doi.org/10.1038/371495a0>
- Nakamura, R., Baumjohann, W., Asano, Y., Runov, A., Balogh, A., Owen, C. J., et al. (2006). Dynamics of thin current sheets associated with magnetotail reconnection. *Journal of Geophysical Research*, *111*(11), 1–14. <https://doi.org/10.1029/2006JA011706>
- Pritchett, P. L. (2015). Structure of exhaust jets produced by magnetic reconnection localized in the out-of-plane direction. *Journal of Geophysical Research: Space Physics*, *120*(1), 592–608. <https://doi.org/10.1002/2014JA020795>
- Pucci, F., Usami, S., Ji, H., Guo, X., Horiuchi, R., Okamura, S., et al. (2018). Energy transfer and electron energization in collisionless magnetic reconnection for different guide-field intensities. *Physics of Plasmas*, *25*(12), 122111. <https://doi.org/10.1063/1.5050992>
- Ricci, P., Brackbill, J. U., Daughton, W., & Lapenta, G. (2004). Collisionless magnetic reconnection in the presence of a guide field. *Physics of Plasmas*, *11*(8), 4102–4114. <https://doi.org/10.1063/1.1768552>
- Shu, Y., Lu, S., Lu, Q., Ding, W., & Wang, S. (2021). Energy budgets from collisionless magnetic reconnection site to reconnection front. *Journal of Geophysical Research: Space Physics*, *126*(10). <https://doi.org/10.1029/2021JA029712>
- Sitnov, M. I., Merkin, V. G., Roytershteyn, V., & Swisdak, M. (2018). Kinetic dissipation around a dipolarization front. *Geophysical Research Letters*, *45*(10), 4639–4647. <https://doi.org/10.1029/2018GL077874>
- Sitnov, M. I., Swisdak, M., & Divin, A. V. (2009). Dipolarization fronts as a signature of transient reconnection in the magnetotail. *Journal of Geophysical Research*, *114*(A4). <https://doi.org/10.1029/2008ja013980>
- Song, L., Zhou, M., Yi, Y., Deng, X., Zhong, Z., & Man, H. (2020). Force and energy balance of the dipolarization front. *Journal of Geophysical Research: Space Physics*, *125*(9), 1–11. <https://doi.org/10.1029/2020JA028278>
- Tharp, T. D., Yamada, M., Ji, H., Lawrence, E., Dorfman, S., Myers, C. E., & Yoo, J. (2012). Quantitative study of guide-field effects on hall reconnection in a laboratory plasma. *Physical Review Letters*, *109*(16), 2–6. <https://doi.org/10.1103/PhysRevLett.109.165002>
- Vapirev, A. E., Lapenta, G., Divin, A., Markidis, S., Henri, P., Goldman, M., & Newman, D. (2013). Formation of a transient front structure near reconnection point in 3-D PIC simulations. *Journal of Geophysical Research: Space Physics*, *118*(4), 1435–1449. <https://doi.org/10.1002/jgra.50136>
- Wang, L., Huang, C., Cao, X., Du, A., & Ge, Y. S. (2020). Magnetic energy conversion and transport in the terrestrial magnetotail due to dipolarization fronts. *Journal of Geophysical Research: Space Physics*, *125*(10), 1–11. <https://doi.org/10.1029/2020JA028568>
- Wu, P., & Shay, M. A. (2012). Magnetotail dipolarization front and associated ion reflection: Particle-in-cell simulations. *Geophysical Research Letters*, *39*(8), 1–5. <https://doi.org/10.1029/2012GL051486>
- Wu, P., Shay, M. A., Phan, T. D., Oieroset, M., & Oka, M. (2011). Effect of inflow density on ion diffusion region of magnetic reconnection: Particle-in-cell simulations. *Physics of Plasmas*, *18*(11), 11204. <https://doi.org/10.1063/1.3641964>
- Xu, J., Peng, F. Z., Russell, C. T., Giles, B., Lindqvist, P.-A., Torbert, R. B., et al. (2020). Observation of energy conversion near the X-line in asymmetric guide-field reconnection. *The Astrophysical Journal*, *895*(1), L10. <https://doi.org/10.3847/2041-8213/ab8e31>
- Yamada, M., Kulsrud, R., & Ji, H. (2010). Magnetic reconnection. *Reviews of Modern Physics*, *82*(1), 603–664. <https://doi.org/10.1103/RevModPhys.82.603>
- Yamada, M., Levinton, F. M., Pomphrey, N., Budny, R., Manickam, J., & Nagayama, Y. (1994). Investigation of magnetic reconnection during a sawtooth crash in a high-temperature tokamak plasma. *Physics of Plasmas*, *1*(10), 3269–3276. <https://doi.org/10.1063/1.870479>
- Yamada, M., Yoo, J., Jara-Almonte, J., Daughton, W., Ji, H., Kulsrud, R. M., & Myers, C. E. (2015). Study of energy conversion and partitioning in the magnetic reconnection layer of a laboratory plasma. *Physics of Plasmas*, *22*(5), 056501. <https://doi.org/10.1063/1.4920960>
- Yamada, M., Yoo, J., Jara-Almonte, J., Ji, H., Kulsrud, R. M., & Myers, C. E. (2014). Conversion of magnetic energy in the magnetic reconnection layer of a laboratory plasma. *Nature Communications*, *5*(May), 4774. <https://doi.org/10.1038/ncomms5774>
- Yi, Y., Zhou, M., Song, L., & Deng, X. (2019). On the energy conversion rate during collisionless magnetic reconnection. *The Astrophysical Journal*, *883*(1), L22. <https://doi.org/10.3847/2041-8213/ab40c1>
- Yi, Y., Zhou, M., Song, L., & Deng, X. (2020). Energy conversion during multiple X-lines reconnection. *Physics of Plasmas*, *27*(12), 122905. <https://doi.org/10.1063/5.0018269>
- Yoon, P. H., & Lui, A. T. Y. (2008). Drift instabilities in current sheets with guide field. *Physics of Plasmas*, *15*(7), 072101. <https://doi.org/10.1063/1.2938386>
- Zhong, Z. H., Deng, X. H., Zhou, M., Ma, W. Q., Tang, R. X., Khotyaintsev, Y. V., et al. (2019). Energy conversion and dissipation at dipolarization fronts: A statistical overview. *Geophysical Research Letters*, *46*(22), 12693–12701. <https://doi.org/10.1029/2019GL085409>
- Zhong, Z. H., Zhou, M., Liu, Y.-H., Deng, X. H., Tang, R. X., Graham, D. B., et al. (2022). Stacked electron diffusion regions and electron Kelvin–helmholtz vortices within the ion diffusion region of collisionless magnetic reconnection. *The Astrophysical Journal Letters*, *926*(2), L27. <https://doi.org/10.3847/2041-8213/ac4dee>
- Zhou, M., Berchem, J., Walker, R. J., El-Alaoui, M., Goldstein, M. L., Lapenta, G., et al. (2018). Magnetospheric multiscale observations of an ion diffusion region with large guide field at the magnetopause: Current system, electron heating, and plasma waves. *Journal of Geophysical Research: Space Physics*, *123*(3), 1834–1852. <https://doi.org/10.1002/2017JA024517>
- Zhou, M., Deng, X. H., Zhong, Z. H., Pang, Y., Tang, R. X., El-Alaoui, M., et al. (2019). Observations of an electron diffusion region in symmetric reconnection with weak guide field. *The Astrophysical Journal*, *870*(1), 34. <https://doi.org/10.3847/1538-4357/aaf16f>